Research Article Adv. Mater. Lett. 2015, **6**(4), 324-333 ADVANCED MATERIALS Letters

www.amlett.com, www.vbripress.com/aml, DOI: 10.5185/amlett.2015.5661 Published online by the VBRI press in 2015

Shape control synthesis, characterizations, mechanisms and optical properties of large scaled metal oxide nanostructures of ZnO and TiO_2

Rajni Verma[1], Bhanu Mantri[1], Ramphal[1], Avanish Kumar Srivastava[1*]

National Physical Laboratory, Council of Scientific and Industrial Research, Dr. K. S. Krishnan Road, New Delhi 110012, India

[*]Corresponding author. Tel: (+91) 11 45609308; E-mail: aks@nplindia; avanish.aks@gmail.com

Received: 29 October 2014, Revised: 15 December 2014 and Accepted: 24 December 2014

ABSTRACT

In the present study, ZnO and TiO_2 nanostructures of different size have been synthesized in high yield with excellent repeatability by simple, economical and environmentally benign chemical route. ZnO quantum dots and nanorods of tuned aspect ratio were evolved by optimising the reaction conditions such as by varying solvent composition, precursor concentration and by using different additives. On the other hand, the synthesis of brookite, the rare phase, anatase and rutile, the stable phases of TiO_2 were also achieved by just varying the annealing temperature from 400 to 615 °C. The obtained nanostructures were rationalized by various characterization techniques such as XRD, FTIR, Raman, SEM, HR- TEM, UV-Vis and PL. The Phase formation and structure determination were identified by using XRD, FTIR and Raman Spectra, SEM and HR-TEM were performed to determine the morphology and particle size. The aspect ratio was calculated to be in the range of 3.2-9.4 in case of ZnO NRs, and particle size was found to be 2-5 nm for ZnO QDs of wurtzite phase and ~ 10 nm for TiO_2 (anatase phase) NPs, respectively. The UV-Vis optical absorption spectrum demonstrates the band gap value of 3.60, 4.02 and 3.40 eV for ZnO NRs, QDs and TiO_2 NPs respectively. The UV-Vis optical absorption spectrum demonstrates the band gap and room temperature PL spectra illustrates about the various defects present in the sample. Various chemical reactions and mechanism involved in producing these nanostructures are dealt in detail. The future prospective of these metal oxide nanostructures lie in photocatalysis, sensors and biomedical applications. Copyright © 2015 VBRI press.

Keywords: Nanostructures; structural analysis; electron microscopy; spectroscopy.

Rajni Verma has obtained her M.Sc. degree in chemistry from Delhi University in the year 2013. Her current area of research includes synthesis, characterization and application of metal oxide nanostructures, preferably ZnO and TiO_2. Presently, she is working as Project Fellow in National Physical Laboratory (NPL), New Delhi.

Ramphal has completed his M.Tech. in Nanoscience and technology from Kurukshetra University, Kurukshetra. He did his M.Tech. thesis research work at NPL New Delhi. His research interest includes synthesizing various nanomaterials by optimizing the reaction conditions

A.K. Srivastava did a Ph.D. at IISc, Bangalore, (Metallurgy), M.Tech. at IIT, Kanpur (Materials Science) and M.Sc. at IIT, Roorkee (Physics). He has several collaborations of international repute in the field of materials processing and properties, in particular on nanomaterials. He has published more than 175 articles in high impact international journals and presented more than 200 papers in conferences and as invited lectures. He is the recipient of: (i) Metallurgist of the Year Award – 2011 by Minister of Steel, Government of India, (ii) Materials Research Society of India Medal-2011, and (iii) Indian National Science Academy-KOSEF fellowship of the Governments of India & South Korea (2009). He is a fellow of The Indian Institute of Metals.

Introduction

Transition metal oxides receive considerable attention in the research fields of material science, physics, chemistry and biology due to their diverse properties (chemical, electrical, optical, mechanical etc.). As the d-shell of transition metals may not be completely filled, so it gives them a variety of unique properties that make them potentially of great use in electronic devices. These unique properties include wide bandgap, high dielectric constant, good electrical and optical characteristics **[1-3]**. Nanostructures are receiving much attention because of confinement of excitons and phonons due to their smaller size. Recently much attention has been paid to zinc oxide and titanium dioxide, which are inorganic compounds with a wide area of applications and flexibility of preparation in various morphologies with different properties. Synthesis conditions form a vital aspect of the science of nanomaterials, the chemical methods have proved to be more effective and versatile than physical methods. So, in this context, we have synthesized nanostructures of various sizes such as quantum dots, nano-particles and nano-rods by chemical approach.

Zinc Oxide (ZnO) is a wide band gap (3.37eV) n-type semiconductor of II-VI semiconductor group and the tetrahedral coordination of the atoms in wurtzite leads to the absence of a center of symmetry in its crystal. Due to non- centrosymmetry and large electrochemical coupling, it has piezoelectric and pyroelectric properties which lead to its application in mechanical actuators, sensors and resonators **[4-7]**. The existence of its various dimensional morphologies such as nano-wires, -rods, -plates, -flowers facilitates its application in almost every field of research such as in short- wavelength optoelectronics, LEDs, photocatalysis etc. **[8-10]**. Depending on the growth methods and conditions, ZnO nanostructures can emit various colors of light **[11]**. Also, it is bio-compatible material with enhanced antibacterial property. Photocatalytic applications of nano- sized ZnO results in environmental applications **[12]**. Among the various nano-forms, one-dimensional (1-D) oriented nanostructures such as nanorods are particularly important to be used in gas sensors, electrochromic devices, solar cells, capacitors, nano-photonics, nanoelectronics and in efficient field emission. Also, it is chemically sensitive to volatile and other radical gases, therefore ZnO nanomaterials have been used to determine the gas sensing response for various oxidising and reducing gases like ozone, NO_2, NH_3 and H_2S **[13]**. The nanostructures having aspect ratio near one are known as zero dimensional nanostructures such as Quantum Dots (QDs). These nanostructures attract more attention due to the exciton effect which becomes more prominent as an electron-hole pair remains coupled by coulombic attraction **[14]**. The exciton effect becomes more prominent in zero dimensional Quantum dots (QDs). Among the various coventional semiconductor QDs, ZnO QDs are preferred because of low- cost, non-toxicity, tunable fluorescence- range and good photostability **[15, 16]**. Their luminescence, stability and solubility can be tuned by surface decoration techniques **[17]**. Thus, they can be used in various applications such as catalysis, light emitting diodes and biological labels like DNA hybridization, protein conformation analysis and receptor-ligand binding dynamics **[18, 19]**. However ZnO QDs are not stable in aqueous phase as water molecules easily destroy the luminescent centres on the surface but in recent years hydrophilic polymers like 3-aminopropyltrimethoxysilane are used to reduce their limitations **[16, 20]**.

Among the various nano-forms, one-dimensional (1-D) oriented nanostructures such as nanorods are particularly important to be used in gas sensors, electrochromic devices, solar cells, nano-photonics, nanoelectronics and in efficient field emission **[8]**. Therefore, more efforts have been made to synthesize 1-D morphologies by optimizing the reaction conditions to get high yields and good repeatability of ZnO nanostructures.

Titanium dioxide (TiO_2) is the most promising and suitable material due to its superior photocatalytic activity, chemical stability, low cost and non-toxicity **[21-23]**. It has wide applications in dye- sensitized solar cells, air and water purification, antimicrobial activities, sensors **[24, 25]**. TiO_2 exists in the three crystalline forms, brookite, anatase and rutile. At ambient pressure and temperatures, the rutile phase is the thermodynamically stable phase, whereas anatase and brookite are thermodynamically metastable and can be easily converted into stable rutile phase when treated at high temperature. The phase stability depends on the various physical environment and also the interaction between TiO_2 and moisture **[24]**.The three phases of TiO_2 have its own advantages and applications in various fields. Anatase shows the highest photocatalytic activity among the three phases. Generally, nano-sized TiO_2 is characterized by small surface area, small particle size and abundant surface defects. Large surface area and small particle size provide larger surface active sites for photocatalysis. However, at high temperature the growth and agglomeration of nanoparticles results in the decreasing surface area and thus photocatalytic activity reduces greatly **[25]**. Thus we can say that rutile shows the less photocatalytic property.

Here, ZnO and TiO_2 nanostructures have been synthesized successfully. ZnO nanorods and TiO_2 nanoparticles were prepared by sol- gel method which is simple, quick, economical, environmentally benign and low temperature synthesis process. ZnO quantum dots have been synthesized by wet chemical method and characterized by various characterization techniques. The advantages of present field include their potential applications such as photocatalysis, sensors and various biological applications due to their non-toxicity. The objective of current research on ZnO nanorods of different aspect ratios includes the determination of the gas sensing response towards ozone, nitrogen dioxide and ammonia gases for the purpose of human health and environmental protection. As the gas sensing mechanism is the surface reaction so ZnO NRs of different surface to volume ratio will show different results. Quantum dots will be utilized to make it more suitable for biomedical applications. Zero dimensional (0-D) TiO_2 NPs will be used as starting points for more complex materials with enhanced properties. Novelty of current research includes the production of ZnO NRs in high yield with high aspect ratio, which can further be used in above mentioned applications and ZnO QDs having size less than Bohr excitonic radius. The three

phases of TiO_2, brookite, the rare phase and anatase and rutile, the stable phases, have been obtained by just varying the annealing temperature.

Experimental

Chemicals

The chemicals used in the synthesis of ZnO nanostructures, both nanorods and quantum dots, are zinc acetate dihydrate ($(Zn(CH_3COOH)_2.2H_2O$, LR, 98%, Thomas Baker Pvt. Ltd., India), methanol (CH_3OH, AR, 99.8%, Rankem, India), sodium borohydride ($NaBH_4$, LR, 98%, Acros Organics, USA), hydrogen peroxide (H_2O_2, LR, 30%, Rankem, India), polyvinyl alcohol (PVA, LR, 75%, Central Drug House Pvt. Ltd., India) and polyvinyl pyrrolidone (PVP, LR, Sigma Aldrich USA). For TiO_2 nanoparticles, titanium tetra isopropoxide ($Ti(OCH(CH_3)_2)_4$, LR, 98%, Spectrochem Pvt. Ltd., India) was used. All chemicals were used without further purification. Absolute ethanol (C_2H_6O, AR, 99.9%, S D Fine-Chem Ltd., India) and millipore water (18 MΩ) was used during the synthesis process and further characterizations.

Synthesis of ZnO and TiO_2 nanostructures

ZnO nanorods (ZnO NRs): ZnO nanostructures were obtained by sol- gel method using easily available precursor of zinc i.e. zinc acetate dihydrate and different solvent compositions. Firstly, 0.3 M of the precursor was added to the 91g of mixed ethanol: water (100: 0) solvent and it was magnetically stirred to get the homogeneity. Now the temperature was changed to 69 °C to get the homogeneous sol. The transformation of sol to gel is called gelation. Here, gelation takes place when the temperature was raised to 93 °C.

Once the gel was formed, it was dried at room temperature and calcined at 400 °C for 4 h at a constant heating rate of 10 °C/min inside a muffle furnace to get the final morphology. Various experimental reaction conditions used to prepare different samples have been tabulated in **Table 1**.

Table 1. Parameters used during synthesis of ZnO nanorods.

Sample detail	Precursor Concentration	Additives Used	Solvent (ethanol : H_2O)
S1	0.3 M	Nil	100 : 0
Effect of Additives			
S2	0.3 M	PVA (3 g)	100 : 0
S3	0.3 M	PVA (3 g) + PVP (1%)	100 : 0
S4	0.3 M	PVA (3 g) + PVP (2%)	100 : 0
Effect of Solvent			
S5	0.3 M	PVA (3 g)	70 : 30
S6	0.3 M	PVA (3 g)	30 : 70
Effect of Precursor Concentration			
S7	0.5 M	PVA (3 g)	100 : 0
S8	0.1 M	PVA (3 g)	100 : 0

ZnO quantum dots (ZnO QDs): ZnO QDs were prepared by wet chemical methods using zinc acetate dihydrate and methanol. In a typical process, methanol (80 ml) was added to the zinc acetate dihydrate (~0.001 M) and it was then stirred and heated continuously. Sodium borohydride (0.2 g) was then added to the mixture, followed immediately by the addition of hydrogen peroxide (4 ml). A white suspension obtained was collected, centrifuged and washed with ethanol and finally dried at 60 °C for 6 h in a vacuum oven.

TiO_2 nanoparticles (TiO_2 NPs): TiO_2 NPs were obtained by sol- gel method. In a typical process, TTIP was dissolved in anhydrous alcohol in the ratio of 1:1 by ultrasonic dispersion. 5 ml water was slowly dripped into the mixture, which was stirred for 2 h at ambient temperature. The pH value of the solution was maintained to be 3.0. The solution was aged for 24 h at ambient temperature, followed by filtering, washing for several times with millipore water and anhydrous alcohol, drying at 100 °C for 12 h to form the precursor. Subsequent annealing of precursor at 400, 500 and 615 °C for 2 h in air for the formation of three different phases of TiO_2 NPs.

Characterization

The phase identification and the crystallinity of the samples were measured by using X-ray powder diffraction (XRD) patterns performed on Rigaku bench top X-ray diffractometer using monochromatic Cu-Kα radiation (λ = 1.541 Å) as X-ray source and scanning in 2θ range from 10 to 80°. The structural determination was done by Fourier Transform Infrared Spectroscopy which was recorded with a single- beam Perkin- Elmer (Model Nicolet 5700) FT-IR Model Spectrophotometer. Raman spectrum was collected by laser excitation source of 514 nm using Renishaw inVia Raman spectrometer, UK. The morphological analysis and size of the obtained products were carried out by scanning electron microscope (Zeiss EVO MA-10 SEM operating at 10.0 keV). The high-resolution transmission electron microscopy analysis was performed by using a HRTEM (FEI Tecnai G2 F30 STWIN operating at 300 keV). Samples were prepared by dispersing them into the ethanol and then a drop of dispersed sample was placed on carbon-coated copper grid. It was then evaporated immediately at ambient temperature. The UV-Vis adsorption spectra of the metal oxide products were collected using a UV–Vis spectrometer (UV-2401 PC, Shimadzu Corporation Japan). The room temperature photoluminescence (PL) investigations were performed using a Perkin Elmer LS-55 fluorescence spectrophotometer with a Xenon (Xe) lamp as the source of excitation.

Results and discussion

ZnO NRs: Phase identification and morphology analysis

The phase identification and morphology investigation of ZnO nanorods (NRs) are depicted in **Fig. 1(a-i)**. The XRD data were recorded in 2θ range from 30-80°. **Fig. 1(a)** shows the sharp diffraction peaks $(10\bar{1}0)$, (0002), $(10\bar{1}1)$, $(10\bar{1}2)$, $(11\bar{2}0)$, $(10\bar{1}3)$, $(11\bar{2}2)$ and $(20\bar{2}0)$ confirming the hexagonal crystal system and wurtzite phase of ZnO with space group 186 (*P63mc*), possessing lattice parameters of a = b = 0.325 nm and c = 0.520 nm (standard JCPDF-ICDD card no.: 36-1451). No peaks were detected corresponding to impurity or the remnant of zinc acetate or

zinc hydroxide, signifying the successful completion of the reaction. Strong intensity and narrow width peaks indicate the highly crystalline structure of ZnO NRs. The crystallite size was calculated using Debye-Scherrer formula in the range of 24-37 nm. The XRD analysis of all the samples was found to be same and it reveals that all the samples show strongest (0002) and $(10\bar{1}0)$ peaks and preferred orientation with c-axis growth.

FTIR spectrum **(Fig. 1(b))** is generated by the absorption of electromagnetic radiation in the frequency range 4000 to 400 cm^{-1}. Different functional groups absorb at characteristic frequency and thus it is used to identify the various functional groups and the bonding present in the sample. The broad band at 3688 cm^{-1} corresponds to O-H group probably due to the atmospheric moisture. The peak frequencies at 2308 and 2099 cm^{-1} are attributed to the asymmetric stretch of CO_2. The bands at 1566 and 1375 cm^{-1} correspond to asymmetric and symmetric stretching vibration of $-COO^-$ of acetate group, respectively **[26]**. The characteristic peak at 695 cm^{-1} corresponds to M-O stretching mode, where M is Zn metal here **[27]**.

SEM was used to evaluate the fine-scaled topological features of the samples. SEM micrographs at different magnifications are shown in the **Fig. 1(c1-c8)** for the ZnO samples S1-S8, respectively. It is clear from the micrographs that the growth of NRs occurs towards top, (0001) plane rather than any other side plane. It may be due to its higher surface energy that the rate of anisotropic growth is higher at this plane **[28]**. For S1, when zinc acetate dihydrate reacts with ethanol, zinc oxide is formed (as confirmed by XRD; **Fig. 1(a)**), but rod like morphology is not observed. As in this sample no PVA or PVP was used, the initial stage of the formation of nanorods can be seen instead of the formation of nanoparticles. It is well known that the addition of polymer alters the morphology and size of crystallites, thus in S2 the addition of PVA causes the anisotropic growth of NRs in only one direction which converts these nanostructures to one dimensional NRs.

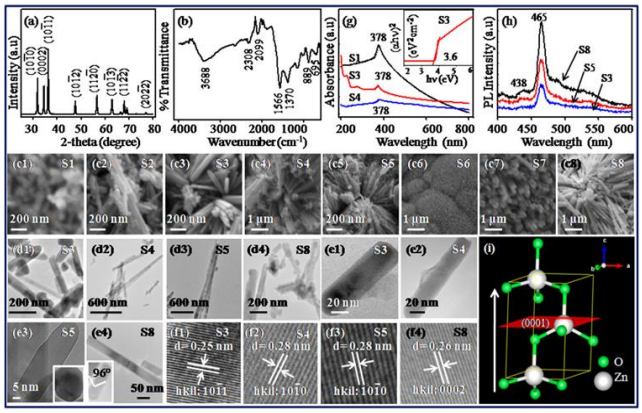

Fig. 1. (a) XRD pattern, (b) FTIR spectrum, (c1-c8) SEM micrographs, (d1-d4) and (e1-e4) TEM images at low and high magnification, respectively, (f1-f4) lattice-resolved HRTEM images, (g) UV-vis, and (h) PL spectra of ZnO nanorods synthesized at various conditions. Insets in (e1 and e4) provide the nano-hexagon and triangular terminated nanorod, respectively, (g) demonstrates the Tauc plot for the corresponding sample. (i) illustrates the crystallographic ball-and-stick model of hexagonal ZnO; color code: green (small) balls indicate oxygen atoms, and white (large) balls signify zinc atoms, and red rectangle represents (0001) plane.

After the addition of PVA, the magnetic stirring helps to initiate high shear flow and thus PVA becomes fully oriented in one direction **[29]**. This occurs because of these reasons: (i) the addition of capping molecule helps to alter the surface energy of crystallographic surface as PVA tends to get adsorb to a particular crystallographic plane **[30]** (ii) as the temperature of semi-crystalline PVA **[31]** becomes higher than the glass transition temperature, Tg **[32]**, the movement of polymer segments enhances and thus the polymer starts interacting with the zinc ions. (iii) the addition of PVA helps the formation of polymer matrix which not only act as template but also provides a barrier against agglomeration and thus imparts stability. So, PVA acts as both a gelator and stabilizing agent. In S3, both the PVA and PVP are used. Amphiphilic PVP has two electron rich species, oxygen and nitrogen so it can use any of these species to interact with nanostructures. But as oxygen of carbonyl group is free so, nanoparticles are supposed to interact with oxygen. The interaction made between hydroxyl group of PVA and carbonyl group of PVP is called hydrogen bonding **(Scheme 1)**. Thus hydrogen bonding formed between zinc hydroxide and hydrophilic polymer restricts their mobility and hence slow growth of nanostructures occur **[33]**. In sample S4, more concentration of PVP was used that helps in de-agglomeration compared to non- capped nanostructures. Also, the growth of NRs in S4 was found to be enhanced. The reason behind the formation of de-agglomerated S3 sample as compared to S4 is that lesser hydrogen bonding occurs due to lesser concentration of PVP used.

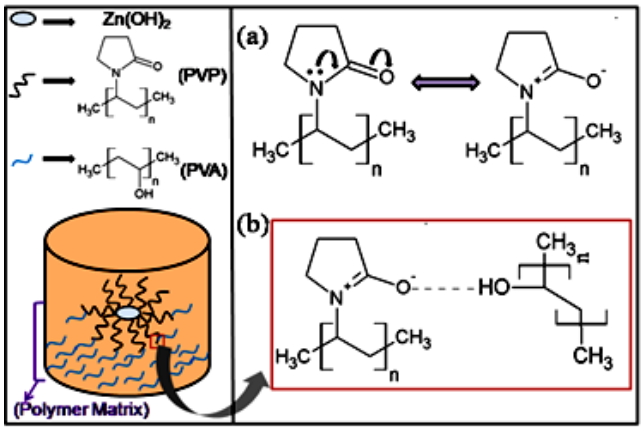

Scheme 1. (a) Resonance occurs in PVP and (b) H-bonding between carbonyl group of PVP and hydroxyl group of PVA.

Samples S5 and S6 have been prepared by changing the solvent composition. Solvent polarity plays a very important role in nucleation and crystal growth process **[34]**. In low polarity solvent such as ethanol, zinc acetate dihydrate get readily dissolves. Thus, it is the reason that in ethanol: water (70: 30), the nucleation and crystal growth along [0002] plane occurs resulting in rod like morphology. However, the obtained length and diameter of NRs of S5 is less than that obtained from S3 indicating that more the amount of ethanol is used, more the length of NRs obtained. Further addition of water used as solvent (S6), the larger the grain like particle morphology was observed and very small nanorods are bulging outward which can clearly

be seen at higher magnification. This is because in the solvent of higher polarities, zinc acetate does not dissolve completely and thus nucleation leads to the growth of crystal transversely. Samples S7 and S8 were synthesized by varying the concentration of the precursor which affects the morphology of ZnO nanostructures. At higher concentration of 0.5 M, micro sized rods are observed whereas nanorods with high aspect ratio are observed when low concentration of precursor is used. It may be because at low concentration, slow nucleation leads to increase in the growth of NRs.

TEM is the powerful technique for further analyzing the topography of nanostructures. Obtained nanorods were characterized by TEM for better understanding of the formation mechanism as represented in **Fig. 1(d1-e4)**. Particle size and lattice fringes with d- spacings can be calculated.

The aspect ratio of the samples, S3, S4, S5 and S8 has been briefly tabulated in **Table 2**. The lattice spacing of S3 is 0.25 nm which is in good agreement with $[10\bar{1}1]$ plane and S4, S5 is 0.28 nm belongs to $[10\bar{1}0]$ plane of wurtzite phase of ZnO obtained from XRD pattern, as shown in HR-TEM images of **Fig. 1(f1-f4)** . The ultrafine nanocrystals reveal high crystallinity and monodispersity.

Table 2. Aspect ratio of ZnO NRs obtained from TEM micrographs.

Sample details	Length (0001) plane	Diameter $10\bar{1}0$ plane	Aspect Ratio (0001/ $10\bar{1}0$)
S3	101	31	3.26
S4	145	30	4.83
S5	91	29	3.14
S8	404	43	9.40

Optical properties

It is generally accepted that the optical transition arises when a photon is absorbed or emitted by the defect. Therefore, optical absorption and luminescence emission property was studied to know the presence of intrinsic point defects. The energy gap of the samples could be estimated by Tauc equation, which is-

$$\alpha h\nu = A(h\nu - Eg)^{1/n}$$

where, α is the absorption coefficient, A is the proportionality constant, hν is the energy of discrete photon, n is equal to 2 for direct transition and ½ for indirect transition **[35]**. The energy band gap is obtained by drawing a tangent to touch the x- axis of the curve showing the variation of $(\alpha h\nu)^2$ with absorption energy (hν). For ZnO nanorods, the band gap was found to be 3.6 eV, as illustrated in **Fig. 1(g)**.

PL spectra provide the information about defects and surface oxygen vacancies as well as excitonic recombination so it is used to determine the electronic structure and optical characteristics of the semiconductor nanomaterials. PL spectra directly arise from the radiative recombination processes of electron and hole between the two energy states and thus it is used to determine the charge recombination rate. The recombination rate of photogenerated electron and hole is directly proportional to the intensity of PL emission **[36]**. PL of ZnO consists of two phenomena: UV emission arising from the band gap transition and Visible emission coming from oxygen vacancies **[29]**. The UV emission band arises due to the photo- generated electron recombination with the holes present in the valence band and Visible emission arises due to the recombination of an electron with a hole present in deep trap or it can be due to the recombination of electron with photo- generated hole in the valence band. The room temperature PL spectra of various samples at the excitation wavelength of 333 nm is shown in the **Fig. 1(h)**. As we know that the intensity of the peak depends on the concentration of the defects present in the sample. Thus the strong and dominating peak in the visible region shows not only the high concentration of oxygen vacancy in ZnO nanorods but also the high surface-to-volume ratio of triangular terminated NRs (sample S8) **[37]**. As XRD pattern does not show the peak of any other material except ZnO and thus it can be assumed that the visible emissions are seen due to intrinsic defects **[11]**. The blue emission around 438 and 465 nm arise due to intrinsic defects, particularly interstitial zinc (Zn_i) which may be due to the stoichiometry of ZnO.

Thus, ZnO (wurtzite) NRs have been synthesized in high yield by optimizing the various reaction conditions. PL intensity at 465 nm was highest for the sample prepared at a low precursor concentration than other samples as it has a high aspect ratio of 9.4 as elucidated by HR-TEM which can further be used in sensors and other applications **[13]**.

ZnO QDs

Structural and optical property analysis: The XRD pattern of ZnO QDs is represented in **Fig. 2(a)**. It shows only four broad peaks as the size of QDs is very small. The diffraction peaks can be indexed as, $(10\bar{1}0), (10\bar{1}1), (11\bar{2}0), (10\bar{1}3)$ which belongs to the JCPDS-ICDD card no.-36-1451 showing wurtzite phase and hexagonal crystal system. From the Debye-Scherrer equation, which correlates the peak broadening with the size of the quantum dot, the average crystallite diameter was found to be 2-3 nm. The crystallite size becomes smaller and crystallinity becomes more when QDs are compared with the nanorods. Also, it is obvious that the width and intensity of diffraction peaks changed markedly with the change in size of nanostructures. The diffraction peak broadening is mainly due to the four factors: microstrains (deformation of the lattice), faulting (extended defects), crystalline domain size and domain size distribution **[38]**. If we assume that the obtained product is free of any strain and the peak broadening is only because of the crystallite size domain, then the average crystallite size can be calculated by Debye- Scherrer equation. The typical optical transmittance spectrum of ZnO is depicted in **Fig. 2(b)**. The broad band at 3489 cm^{-1} is the O-H bond stretching. The peak at 1044 and 429 cm^{-1} correspond to C-O and Zn-O stretch, respectively. Quantum confinement effect causes PL blue shift of QDs. PL emission spectrum **(Fig. 2(c))** shows the emission peak in visible region at

407, 436 and 464 nm when λ of excitation was taken to be 310 nm. The band in the ultraviolet emission corresponds to near band edge excitonic emission and the bands in the visible region, 407, 436 and 465 nm, are related to the Zn defects present in ZnO QD. The PL excitation spectrum (shown in the inset) indicates sharp peak at 310 nm when λ of emission was taken to be 464 nm. As we know that when sufficient energy of specific wavelength falls on the QDs, the electrons from the valence band excite to the conduction band leaving behind a mobile positive hole in the valence band. After excitation, electron and hole lose their energy and jumps at the bottom of the conduction band and the top of the valence band, respectively. Thus, the energy is released when an electron recombines with a hole. This released energy is the sum of the confinement energies of the excited electron and hole, the band gap energy and the bound energy of the exciton **[14, 39]**.

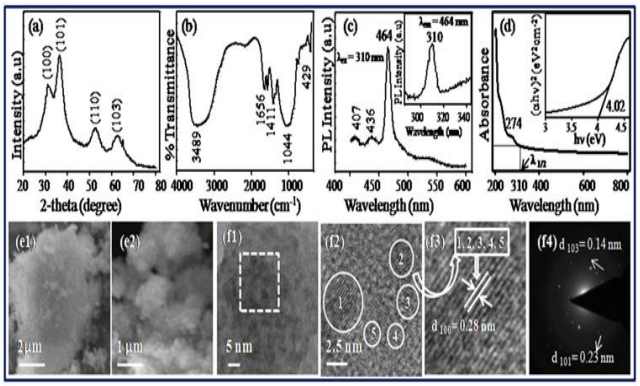

Fig. 2. (**a**) XRD spectrum, (**b**) Optical transmittance spectrum, (**c**) PL emission spectrum, (**d**) UV-Vis spectrum, (**e1**)-(**e2**) SEM micrographs, (**f1**)-(**f4**) TEM images, where (**f1**) represents the TEM micrograph at low magnification, (**f2**) shows the morphology and size of QD, (**f3**) illustrates lattice resolved HRTEM image, (**f4**) SAED ring pattern. Insets in (**c**) and (**d**) tells the PL excitation spectrum at λ em 464 nm and optical band gap obtained from tauc plot, respectively.

The size of ZnO QDs can be obtained by the following equation **[40]**:

$$1240/\lambda_{1/2} = 3.301 + 294/D^2 - 1.09/D$$

Where, $\lambda_{1/2}$ is the wavelength at which the absorption is 50% to that of the excitonic peak which is 310 nm as shown in the **Fig. 2(d)**, where D is the size obtained in Å.

So, the calculated size of QD was found to be 2 nm which is in good agreement with HRTEM result. Therefore, QDs are having size less than that of the bohr excitonic radius and thus the electron and holes are confined, leading to so- called Quantum Confinement Effect where energy levels are discrete and quantized, with value directly depends on nanocrystal size. Here, ZnO QDs absorbs in UV-C region indicating the blue shift compared to ZnO NRs due to quantum confinement effect. The lowest band gap energy required to create an electron-hole pair i.e. the band gap energy was found to be 4.02 eV. The band gap broadens as size decreases.

Morphology and particle size determination

The SEM micrographs at different magnifications have been represented in **Fig. 2(e1, e2)**. It is clear from the images that the particles are uniformly distributed and very small in size. For better analysis of QD morphology, TEM was used as shown in the **Fig. 2(f1-f4)**.

The TEM image at low magnification **(Fig. 2(f1))** elucidates high agglomeration of ZnO QDs as shown by a square. The **Fig. 2(f2)** clearly reveals the nearly spherical QDs of size varying between 2-5 nm obtained at high magnification. As we know that the Bohr exciton radius, a_B of ZnO is 2.34 nm, so the nanostructure when approaches this size is supposed to show quantum confinement effect **[41]**. In order to even distinguish it more clearly, HRTEM was carried out. The HR-TEM image **(Fig. 2(f3))** shows highly resolved lattice d-spacing of 0.28 nm corresponds to [100] plane of wurtzite ZnO. The crystallinity of ZnO QDs is also demonstrated by the electron diffraction pattern obtained in HR-TEM. SAED pattern, as depicted in **Fig. 2(f4)**, represents the diffraction rings which are indexed to hexagonal wurtzite phase of ZnO which is in agreement with XRD pattern.

ZnO QDs have been synthesized by wet chemical method and the estimated size was found to be less than Bohr excitonic radius which was in the range of 2-5 nm as conformed by HR-TEM results.

TiO_2 NPs

Structure identification and morphology investigation: The X-ray diffraction pattern of TiO_2 is shown in **Fig. 3(a)** which demonstrates the formation of different phases at different annealing temperature. As the annealing temperature increases the brookite phase converts into anatase which further converts into rutile phase. The diffraction peaks **(Fig. 3(a1))** obtained, when the gel was calcined at 400 °C, are in agreement with brookite (JCPDF ICDD card no- 76-1936) of orthorhombic crystal system and having space group - *Pbca* (61) with lattice parameters, a= 9.191, b= 5.463 and c = 5.157. The diffraction peaks **(Fig. 3(a2))** observed when the annealing temperature was changed to 500 °C, match exactly with anatase phase (JCPDF ICDD card no. 73-1764) having cell parameters as a=b= 3.776 and c = 9.486. When the temperature was raised to 615 °C, the rutile phase (JCPDF ICDD card no. 73-1765) with some amount of anatase phase was observed **(Fig. 3(a3))** which shows that the anatase phase is not completely converted into rutile phase. Star symbols in this figure represent the rutile phase present in this sample. The % of phase content present in the sample can be calculated from the equation using integrated intensities **[42]**. The % of anatase and rutile were found to be 51 and 49%, respectively. Also the peaks become narrow with increase in temperature indicating the improvement in crystallinity and increase in size. The estimate grain size obtained is ~10 and 15 nm for brookite and anatase, respectively as calculated by Debye Scherrer equation. The grain size obtained from XRD is in agreement with the diameter of nanostructures obtained from TEM. Since the crystallite size is small, the oxygen defects are closely packed and thus they interact resulting in the formation of comparatively larger nuclei which is the reason of anatase conversion to rutile at higher temperature **[43]**. The crystallite size of rutile was found to be ~34 nm showing that at higher temperature, removal of grain boundary defects occur resulting to the increase in crystallite size.

Raman peaks originate from the vibration of the molecular bonds, that is, vibrational mode E_g and A_{1g} peaks, which is related to different crystal plane. Therefore it provides the high accuracy and sensitivity for measuring the percentage of the exposed facets from the micro perspective of molecular bonding with less measured errors. Raman spectra were performed from raman shift of 200 to 800 cm^{-1} at the excitation line of 514 nm, as shown in the **Fig. 3(b)**. When raman spectroscopy was applied to characterize the TiO_2 nanoparticles, it has been known that the E_g peak is mainly caused by symmetric stretching vibration of O—Ti—O in TiO_2, B_{1g} peak is caused by symmetric bending vibration of O— Ti—O and A_{1g} peak is caused by antisymmetric bending vibration of O—Ti—O. Raman spectroscopy is a form of vibrational spectroscopy, much like infrared (IR) spectroscopy. It exhibits high specificity and is compatible with aqueous and solid systems. No special preparation of the sample is needed, and the timescale of the experiment is short. All Raman spectra were recorded at room temperature. The strong raman peaks of brookite can be seen at 395, 446 and 637 cm^{-1}, where the peak at 395 cm^{-1} corresponds to B_{2g} and at 636 cm^{-1} corresponds to A_{1g} **[44]** as depicted in **Fig. 3(b1)**. The major raman bands at 398, 517 and 640 cm^{-1} confirm the anatase crystal phase of TiO_2 as shown in the **Fig. 3(b2)**. These bands can be attributed to raman active modes of anatase phase with the symmetries of B_{1g}, A_{1g} and E_g, respectively. The thermodynamically stable rutile phase exhibits major peaks at 397, 515 and 638 cm^{-1} and minor peak at 247 cm^{-1} as represented in **Fig. 3(b3)**. The 1st peak at 247 cm^{-1} corresponds to rutile phase **[45]** and remaining peaks correspond to anatase phase which shows that this sample contain both the phase rutile and Anatase and rutile phase is at the initial stage of forming at 615 °C **[46]** as confirmed by XRD. As we know that raman spectra depends on the finite size of nanoparticles, so new bands can be observed with increase in surface-to-volume ratio i.e with decrease in particle size **[47]**.

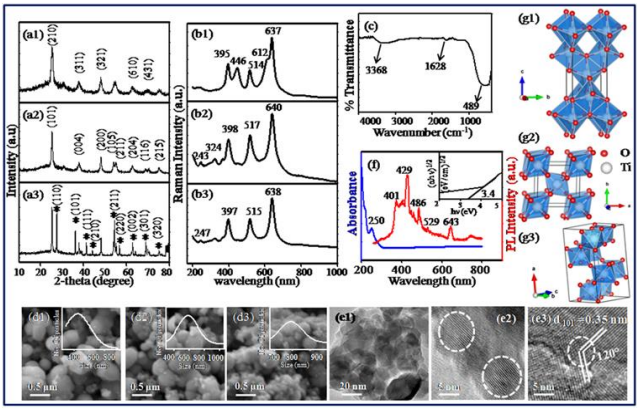

Fig. 3. (a1)-(a3) XRD images, (b1)-(b3) Raman spectra of brookite, anatase and rutile, respectively, (c) FTIR spectrum, (d1)-(d3) SEM micrographs, (e1) TEM image at low magnification, (e2) HR-TEM image showing size of anatase particles, (e3) lattice resolved HRTEM image, dotted circle represents overlapping of crystal planes, (f) mixed graph of UV-Vis and PL of anatase phase, (g1)-(g3) 3D polyhedral models of anatase, rutile and brookite, respectively, color code: red (small) balls indicate oxygen atoms, and white (large) balls signify titanium atoms. The symbol of star in (a3) indicates the rutile phase.

The FTIR spectrum of TiO_2 is represented in **Fig. 3(c)**. A broad band between 3200 to 3800 cm^{-1} was observed which is related to stretching hydroxyl (O-H) group, representing the water present as moisture **[48]**. The other peak at 1628 cm^{-1} were indicated to stretching of C=O bond. The peak observed at 489 cm^{-1} was assigned to Ti-O stretching.

The morphology, of different phases of TiO_2 obtained at different annealing temperatures, does not affected too much from spherical shape but the distribution of particle size changes drastically, as depicted in **Fig. 3(d1-d3)**. The degree of agglomeration is high in all the samples of TiO_2 and it is clear from particle size distribution that spherical size increases as annealing temperature is raised. The reason behind it is that with rise in temperature, the nucleation increases which gives rise to the enhanced growth of particles. TEM images are shown in the **Fig. 3(e1-e3)**. The low magnification TEM micrograph **(Fig. 3(e1))** represents the high degree of agglomeration. HR-TEM image illustrates the d-spacing and also the particle size which was found to be ~10 nm **(Fig. 3(e2 - e3))**.

Optical properties

The absorption wavelength (< 380 nm) is assigned to be the intrinsic band gap absorption of bulk anatase **[49]**. The absorption wavelength of anatase was found to be 250 nm when graph between absorbance vs wavelength was plotted. The band gap of anatase was found to be 3.4 eV which is in agreement with the reported value of anatase phase and it corresponds well with the semiconductor band gap of crystalline bulk anatase.

PL measurement of anatase was made at the excitation wavelength of 251 nm. Analyzing the PL spectra show that there are many defects in the crystal structure due to the presence of various peaks. All peaks correspond to various defect levels in the synthesized sample. At around 380 nm it shows broad shoulder and after that it shows lower energy peaks / shoulders at 2.68, 2.49 and 1.92 eV. The mixed graph of UV-Vis and PL is shown in **Fig. 3(f)**. The high energy peak corresponds to band edge luminescence of anatase and low energy peaks arise due to the presence of oxygen vacancies **[50]**. The peak coming at 486 nm corresponds to the charge transfer transition from Ti^{3+} to oxygen anion associated with oxygen vacancy **[51]**. With the increase of annealing temperature to 615 °C, the number of oxygen vacancies gets reduced as investigated by J.Shi et. Al **[52]**.

TiO_2 NPs of crystallite sizes ~10, 15, and 34 nm for brookite, anatase, and rutile phases, respectively were obtained by sol-gel method. The obtained TiO_2 NPs were used in photocatalysis and other possible applications.

Growth mechanism for the production of high-yield oxides nanostructures

ZnO NRs and QDs: Zinc oxide nanostructures were synthesized by easily available metal precursor. ZnO QDs were prepared by wet chemical method which is simple, fast and environmental benign. In this method, sodium borohydride acts as reducing agent, providing its electrons to the zinc ions, coming from zinc acetate precursor and converting it to the zinc metal. Methanol is used as solvent

which helps in de-agglomeration and also helps for slow and controllable growth of nanostructures. As hydrogen peroxide is a good oxidising agent, so it is used to oxidise the obtained zinc metal. Thus, we can say that ZnO QDs are formed by redox reaction.

ZnO nanorods were obtained by sol gel process which is widely used method for the synthesis of nanostructures. First step in this method is the formation of sol by hydrolysing the metal organic precursor and condensation of small molecules. Next step involves the transformation of obtained sol into an interconnected and rigid like network called gel. This process is called gelation. After gelation, the syneresis of gel occurs which includes the contraction or shrinkage of gel. In aqueous sol – gel process, there occurs nucleophilic attack of oxygen of the water molecule to the metal precursor resulting in the hydrolysis and condensation reaction, whereas intrinsically if no water is present then the oxygen for the formation of oxidic compound is supplied by the solvent (alcohol, ether, ketones etc.) or by the organic constituent of the precursor.

Here, ethanol is used as solvent. As we know that the acetate group can show coordination chemistry with metal through different ways either by coordinating with both the oxygens i.e. bidentate or bridged coordination or it can combine with metal in monodentate fashion. Here, zinc acetate dihydrate combine with metal in bidentate manner and thus the complex is octahedral **[53]**. Zinc acetate dihydrate in the presence of ethanol gets convert into zinc hydroxide as ethanol acts as hydrolysing agent. After that as the temperature changes to 69 °C, homogeneous sol was obtained which on condensing, the small molecules like water, forms gel which gradually changes to white gel on drying. After annealing at 400 °C, the product was obtained because of dehydration **[54]**.

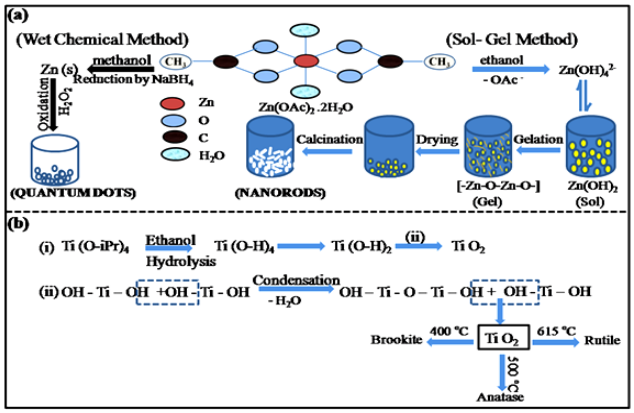

Scheme 2. Schematic representation of the mechanism of ZnO and TiO_2 nanostructures. (a) mechanism of ZnO nanorods formation by sol-gel method and ZnO quantum dots by wet chemical method and (b) mechanism of TiO_2 nanostructures form at various annealing temperatures.

TiO_2 NPs

Brookite, anatase and rutile phases of TiO_2 were obtained by hydrolysing the titanium precursor which is TTIP. Now the obtained titanium hydroxide undergoes self condensation producing titanium dioxide. Obtained TiO_2 gives brookite, anatase and rutile when annealed under 400, 500 and 615 °C, respectively as shown in **Scheme 2**. Pictorial representation of the formation of ZnO NRs under various reaction conditions are depicted in **Scheme 3**.

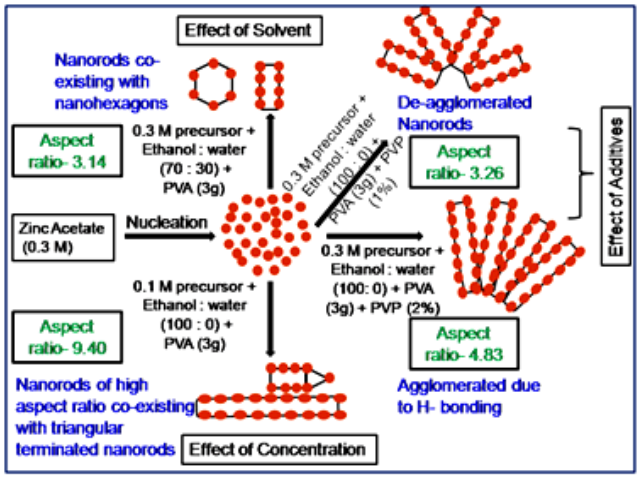

Scheme 3. Pictorial representation of the formation of ZnO nanorods of various aspect ratio under different reaction conditions.

Conclusion

In summary, ZnO NRs of varied aspect ratio were synthesized by optimising the experimental conditions via sol-gel method. ZnO QDs were prepared by wet chemical method and the three phases of TiO_2, brookite, anatase and rutile were obtained by sol-gel method. The selection of starting materials and reaction conditions here we report are very simple, reliable and cost-effective and allows for the production of metal oxide nanostructures in large scale so that they can easily be scaled-up for various applications. High yield product of ZnO and TiO_2 is depicted in **Fig. 4(a** and **b)**. It has been experimentally proved that nature of additives, solvent composition and concentration of precursor play important role to get tunable aspect ratio of NRs. Sample S8, obtained when precursor concentration is decreased, indicates highest PL intensity at 465 nm among other samples as it has highest aspect ratio of 9.4 which is analysed by HR-TEM. The size of ZnO QDs was found to be in the range of 2-5 nm as characterized by UV-Vis which is in good agreement with HR-TEM results. XRD demonstrates the wurtzite phase of ZnO nanostructures. Tauc plot obtained from UV-Vis elucidates the optical band gap of ZnO NRs to be 3.6 eV which increases to 4.02 eV when we talk about QDs. It is concluded that the PL characteristics of nanometer-sized ZnO is responsible to observe blue emission peak. The annealing temperature employed during the synthesis procedure of TiO_2 nanostructures was found to have prominent impact on the evolution of different phases. Various phases of TiO_2 such as brookite, anatase and rutile at annealing temperatures of 400, 500 and 615 °C, respectively were synthesized and tracked by various characterization techniques including XRD, Raman, FTIR, SEM, TEM, UV-Vis and PL spectroscopy. The particle size of spherical shape anatase phase was found to be ~10 nm. The particle size increases with the increase in annealing temperature as depicted by particle size distribution graph. These metal oxide nanostructures of various shapes and sizes can be further used as gas sensors to determine their response towards

ozone, nitrogen dioxide and ammonia gases, photocatalyst and in various biomedical applications.

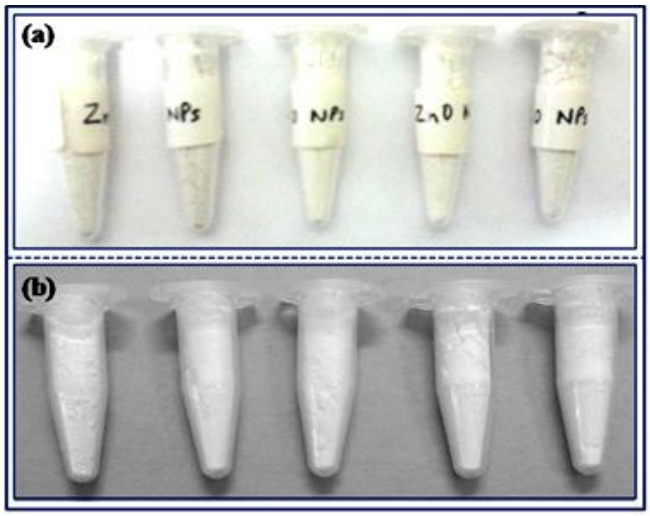

Fig. 4. Large scale synthesis of ZnO and TiO_2 nanostructures. High yield product of (a) ZnO and (b) TiO_2 nanostructures.

Acknowledgements

We thank the Director, NPL New Delhi, India for providing the necessary experimental facilities. Dr. N. Vijayen, Mr. K. N. Sood, Mr. J. S. Tawale, Dr. Ritu Srivastava, Dr. Bhanu Pratap Singh and Dr. D. Haranath are gratefully acknowledged for providing the necessary instrumentation facilities for XRD, FTIR, Raman, SEM, UV-vis and PL. Nano-SHE project (BSC-0112) is gratefully acknowledged.

Reference

1. Kant, S.; Kumar, A.; *Adv. Mat. Lett.*, **2012**, *3(4)*, 350. **DOI:**10.5185/amlett.2012.5344
2. Tawale, J.S.; Kumar, A.; Mohan, A.; Srivastava, A.K.; *Opt. Mater.* **2013**, *35*, 1335. **DOI:**10.1016/j.optmat.2013.01.034
3. Gangwar, J.; Dey, K.K.; Komal, Praveen, Tripathi, S.K.; Srivastava, A.K.; *Adv. Mat. Lett.* **2011**, *2(6)*, 402. **DOI:**10.5185/amlett.2011.3233
4. Dev, A.; Panda, S.K.; Kar, S.; Chakrabarti, S.; Chaudhari, S.; *J. Phys. Chem. B* **2006**, *110*, 14266. **DOI:**10.1021/jp062729l
5. Wang, Z.L.; Song, J.; *Science* **2006**, *312*, 242. **DOI:**10.1126/science.1124005
6. Singh, R.P.; Shukla, V.K.; Yadav, R.S.; Sharma, P.K.; Singh, P.K.; Pandey, A.C.; *Adv. Mat. Lett.* **2011**, *2(4)*, 313. **DOI:**10.5185/amlett.indias.204
7. Tawale, J.S.; Gupta, G.; Mohan, A.; Kumar, A.; Srivastava, A.K.; Sens. Actuators, B **2014**, *201*, 369. **DOI:**10.1016/j.snb.2014.04.099
8. Devan, R.S.; Patil, R.A.; Lin, J.H.; Ma, Y.R.; *Adv. Funct. Mater.* **2012**, *22*, 3326. **DOI:**10.1002/adfm.201201008
9. Chen, Y.W.; Qiao, Q.; Liu, Y.C.; Yang, G.L.; *J. Phys. Chem. C* **2009**, *113*, 7497. **DOI:**10.1021/jp809778w
10. Ji, S S.; Ye, C.; *J. Mater. Sci. Technol.* **2008**, *24*, 457.
11. Ahn, C.H.; Kim, Y.Y.; Kim, D.C.; Mohanta, S.K.; Cho, H.K.; *J. Appl. Phys* **2009**, *105*, 013502. **DOI:** 10.1063/1.3054175
12. Zhang, Y.; Ram, M.K.; Stefanakos, E.K.; Goswami, D.Y.; *J. Nano Mat.* **2012**, Article ID 624520, 22 pages. **DOI:** 10.1155/2012/624520
13. Barreca, D.; Bekermann, D.; Comini, E.; Devi, A.; Fischer, R.A.; Gasparotto, A.; Maccato, C.; Sada, C.; Sberveglieri, G.; Tondello, E.; *Cryst. Eng. Comm.* **2010**, *12*, 3419. **DOI:**10.1039/c0ce00139b
14. Pisanic, T.R.; Zhang, Y.; Wang, T.H.; *Analyst* **2014**, *139*, 2968. **DOI:** 10.1039/c4an00294f
15. Huang, J.J.; Ye, Y.B.; Lei, Z.Q.; Ye, X.J.; Rhong, M.Z.; Zhang, M.Q.; *Phys. Chem. Chem. Phys*. **2014**, *16*, 5480. **DOI:** 10.1039/c3cp55098b
16. Aboulaich, A.; Tilmaciu, C.M.; Merlin, C.; Mercier, C.; Guilloteau , H.; Medjahdi, G.; Schneider, R.; *Nanotechnol.* **2012**, *23*, 335101. **DOI:** 10.1088/0957-4484/23/33/335101
17. Zhou, D.; Lin, M.; Liu, X.; Li, J.; Chen, Z.; Yao, D.; Zhang, H.; Yang, B.; *ACS Nano* **2013**, *7*, 2273. **DOI:** 10.1021/nn305423p
18. Wang, H.P.; Jiang, H.; Wang, X.M.; Chem. Commun. **2010**, *46*, 6900. **DOI:** 10.1039/c0cc00476f
19. Sarkar, S.; Maity, A.R.; Karan, N.S.; Pradhan. N.; *J. Phys. Chem. C.* **2013**, *117*, 21988. **DOI:** 10.1021/jp4035612
20. Moussodia, R.O.; Balan, L.; Merlin, C.; Mustin, C.; Schneider, R.; *J. Mater. Chem.* **2011**, *20*, 1147. **DOI:** 10.1039/b917629b
21. Dutta, R.K.; Sharma, P.K.; Pandey, A.C.; *Adv. Mat. Lett.* **2011**, *2(4)*, 268. **DOI:** 10.5185/amlett.indias.195
22. Muthirulan, P.; Devi, C.K.N.; Sundaram, M. M.; *Adv. Mat. Lett.* **2014**, *5(4)*, 163. **DOI:** 10.5185/amlett.2013.7507
23. Singh, P.; Sinha, O.P.; Srivastava, R.; Srivastava, A.K.; Bindra, J.K.; Singh, R.P.; Kamalasanan, M.N.; *Mater. Chem. Phys.* **2012**, *133*, 317. **DOI:** 10.1016/j.matchemphys.2012.01.030
24. Sang, L.; Zhao, Y.; Burda, C.; Chem. Rev. **2014**, *114*, 9283. **DOI:** 10.1021/cr400629p
25. Jiang, L.; Zhou, W.; Tian, G.; Fu, H.; *Chem. Soc. Rev.* **2013**, *42*, 9509. **DOI:** 10.1039/C3CS60176E
26. Kaviyarasu, K.; Devarajan, P.A.; *Adv. Mat. Lett.* **2013**, *4(7)*, 582. **DOI:** 10.5185/amlett.2012.10443
27. Das, J.; Freitas, F.S.; Evans, I.R.; Nogueira, A.F.; Khushalani, D.; *J. Mater. Chem.*, **2010**, *20*, 4425. **DOI:** 10.1039/b921373b
28. Baxter, J.B.; Walker, A.M.; Ommering, K.V.; Aydil, E.S.; *Nanotechnol.* **2006**, *17*, S304. **DOI:** 10.1088/0957-4484/17/11/S13
29. Kong, K H.; Jang, J.; *Chem. Commun.* **2006**, 3010. **DOI:** 10.1039/b605286j
30. Chen, X.; Mao, S.S.; *Chem. Rev.* **2007**, *107*, 2891. **DOI:** 10.1021/cr0500535
31. Rajeswari, N.; Selvasekarapandian, S.; Prabu, M.; Karthikeyan, S.; Sanjeeviraja, C.; *Bull. Mater. Sci.* **2013**, *36*, 333.
32. Tang, Y.; Zhang, H.; Fan, Z.; Li, M.; Han, J.; Dong, F.; Yang, B.; *Phys. Chem. Chem. Phys.* **2010**, *12*, 11849. **DOI:** 10.1039/c004279j
33. Zhang, H.; Tang, Y.; Zhang, J.; Li, M.; Yao, X.; Li, X.; Yang, B.; rsc, **2009**, *5*, 4113. **DOI:** 10.1039/b914213d
34. Yin, J.; Gao, F.; Wei, C.; Lu, Q.; *Scientific Reports*, **2014**, *4*, 3736. **DOI:** 10.1038/srep03736
35. Bahramian, A.; *Ind. Eng. Chem. Res.* **2013**, *52*, 14837. **DOI:** 10.1021/ie402536h
36. Wu, N.; Wang, J.; Tafen, D.N.; Wang, H.; Zheng, J.G.; Lewis, J.P.; Liu, X.; Leonard, S.S.; Manivannan, A.; *J. Am. Chem. Soc.* **2010**, *132*, 6679. **DOI:** 10.1021/ja909456f
37. Srivastava, A.K.; Deepa, M.; Sood, K.N.; Erdem, E.; Eichel, R.A.; *Adv. Mat. Lett.* **2012**, *2(2)*, 142. **DOI:** 10.5185/amlett.2011.1201
38. Bai, S.; Hu, J.; Li, D.; Luo, R.; Chen, A.; Liu, C.C.; *J. Mater. Chem.* **2011**, *21*, 12288. **DOI:** 10.1039/c1jm11302j
39. Haranath, D.; Sahai, S.; Joshi, P.; *Appl. Phys. Lett.* **2008**, *92*, 233113. **DOI:** 10.1063/1.2944142
40. Yang, Y.; Li, Y.Q.; Fu, S.Y.; Xiao, H.M.; *J. Phys. Chem.* **2008**, *112*, 10553. **DOI:** 10.1021/jp802111q
41. Cho, S.; Jang, J.W.; Lee, J.S.; Lee, K.H.; *Nanoscale*, **2010**, *2*, 2199. **DOI:** 10.1039/c0nr00278j
42. Zhang, H.; Banfield, J.F.; *J. Phys. Chem. B* **2000**, *104*, 3481.

DOI: 10.1021/jp000499j
43. Li, W.; Ni, C.; Lin, H.; Huang, C.P.; Shah, S.I.; *J. Appl. Phys.* **2004**, *96*, 6663.
DOI: 10.1063/1.1807520
44. Rezaee, M.; Khoie, S.M.M.; Liu, K.H.; *Cryst. Eng. Comm.*, **2011**, *13*, 5055.
DOI: 10.1039/C1CE05185G
45. Choudhary, B.; Choudhary, A.; *Int. Nano. Lett.* **2013**, *3*, 55.
DOI: 10.1186/2228-5326-3-55
46. Zhang, J.; Li, M.; Feng, Z.; Chen, J.; Li, C.; *J. Phys. Chem. B* **2006**, *110*, 927.
DOI: 10.1021/jp0552473
47. Choi, H.C.; Jung, Y.M.; Kim, S.B.; *Vib. Spectrosc.*, **2005**, *37*, 33.
DOI: 10.1016/j.vibspec.2004.05.006
48. Gökdemir, F.P.; Yüzbaşıoğlu, V.E.; Keskin, B.; Özdemir, O.; Kutlu, K.; *Adv. Mat. Lett.* **2014**, *5(7)*, 367.
DOI: 10.5185/amlett.2014.amwc.1007
49. Roy, H.G.; *Res. Appl. Mater*. **2013**, *1(6)*, 65.
DOI: 10.12966/ram.09.02.2013
50. Abazovic, N.D.; Comor, M.I.; Dramicanin, M.D.; Jovanovic, D.J.; Ahrenkiel, S.P.; Nedeljkovic, J.M.; *J. Phys. Chem. B*, **2006**, *110*, 25366.
DOI: 10.1021/jp064454f
51. Liu, J.; Li, J.; Sedhain, A.; Lin, J.; Jiang, H.; *J. Phys. Chem C*, **2008**, *112*, 17127.
DOI: 10.1021/jp8060653
52. Shi, J.; Chen, J.; Feng, Z.; Chen, T.; Lian, Y.; Wang, X.; Li, C.; *J. Phys. Chem. C*, **2007**, *111*, 693.
DOI: 10.1021/jp065744z
53. Seguel, G.V.; Rivas, B.L.; Novas, C.; *J. Chil. Chem. Soc.*, **2005**, *50*, N 1.
DOI: 10.4067/S0717-97072005000100006
54. Chang, S.Y.; Yang, N.H.; Hung, Y.C.; Lin, S.J.; Kattamis, T.Z.; Liu, C.Y.; *J. Mater. Chem.*, **2011**, *21*, 4264.
DOI: 10.1039/C0JM03536J

